Wear 606 (2026) 207055

Contents lists available at ScienceDirect

Wear

journal homepage: www.elsevier.com/locate/wear

Process-related tribological and corrosion behavior of additively manufactured 17-4 PH stainless steel

Christian Orgeldinger [a,*], Armin Seynstahl [a], Tobias Rosnitschek [a], Jorge Ramos Grez [b], Magdalena Walczak [b], Max Marian [b,c], Stephan Tremmel [a,d]

[a] Engineering Design and CAD, University of Bayreuth, Universitätsstraße 30, Bayreuth, 95447, Germany
[b] Department of Mechanical and Metallurgical Engineering, School of Engineering, Pontificia Universidad Católica de Chile, Vicuña Mackenna 4860, Región Metropolitana, Macul, 6904411, Chile
[c] Institute for Machine Design and Tribology (IMKT), Leibniz University Hannover, An der Universität 1, Garbsen, 30823, Germany
[d] Bayreuth Center for Material Science and Engineering (BayMAT), Prof.-Rüdiger-Bormann-Str. 1, Bayreuth, 95447, Germany

ARTICLE INFO

Keywords:
Additive manufacturing
Laser beam powder fusion
Metal extrusion additive manufacturing
Atomic diffusion additive manufacturing
Fused filament fabrication
Surface topography

ABSTRACT

The present experimental study investigated the tribological behavior of 17-4 PH stainless steel produced by three different additive manufacturing (AM) processes: laser powder bed fusion (LPBF), atomic diffusion additive manufacturing (ADAM), and metal extrusion additive manufacturing (MEAM), compared to a conventionally manufactured reference. Samples were tested with untreated and polished surfaces under unlubricated, i.e. technically dry, and oil-lubricated sliding conditions with mixed and boundary friction. A statistical surface analysis using ISO 25178 parameters and a principal component analysis enabled a quantitative comparison of AM-specific topographies. Furthermore, microstructure, chemical composition, mechanical properties, friction, wear behavior, and corrosion resistance were comprehensively analyzed. Results showed that surface morphology and porosity strongly influence friction and wear, often more than hardness. Under unlubricated conditions, ADAM exhibited high friction and wear due to sharp surface peaks, despite its high hardness. MEAM showed low friction, likely due to lubricating effects from residual binder. In contrast, in oil-lubricated conditions, ADAM demonstrated negligible wear and the lowest friction, benefiting from its fine porous surface. LPBF achieved high density and wear resistance but showed the lowest corrosion pitting resistance due to larger surface defects. The study emphasizes that tribological performance in AM components is strongly process-dependent and must be assessed holistically. The presented methodology provides a framework for selecting and optimizing AM processes for components that are also subjected to tribological and possibly corrosive influences.

1. Introduction

Additive manufacturing (AM) has gained momentum as an innovative solution for producing geometrically complex shaped, high-performance components across various sectors, from aerospace over industrial to biomedical applications [1]. Unlike traditional manufacturing techniques, AM allows for near-net-shape production with minimized waste and increased flexibility in part geometry, enabling energy-efficient production. Furthermore, AM's capacity to tailor material properties and minimize environmental impact aligns well with modern sustainability goals, as energy and material efficiency are essential to a green transition in the industry [2]. While polymers continue to account for a large share of the AM market, metallic AM is becoming increasingly important for highly loaded engineering applications. Metal AM processes can generally be categorized into powder-bed fusion techniques, such as LPBF, and material extrusion routes, where metal-powder-filled filaments are printed and subsequently debound and sintered to form dense metallic components [3–6]. These manufacturing routes differ fundamentally in their thermal history, consolidation mechanisms, and resulting microstructures, which may influence tribological performance [7].

In all the metal AM processes, the material is added layer by layer through repeated cycles of melting and solidification. This cyclic thermal process, involving rapid heating, melting, and cooling, leads to a

* Corresponding author.
E-mail address: christian.orgeldinger@uni-bayreuth.de (C. Orgeldinger).

https://doi.org/10.1016/j.wear.2026.207055
Received 18 June 2026; Received in revised form 8 September 2026; Accepted 18 September 2026
Available online 19 September 2026
0043-1648/© 2026 The Authors. Published by Elsevier B.V. This is an open access article under the CC BY license (http://creativecommons.org/licenses/by/4.0/).
Open access funding enabled and organized by Projekt DEAL.

complex thermal history for each layer. As a result, the roughness of AM-produced parts is characterized by irregular, stochastic patterns [8]. This irregular surface topology often results in lower surface quality compared to conventionally manufactured parts, which impacts the mechanical performance and efficiency of AM components in various applications [9]. The durability of metal AM components is often hindered by wear issues, necessitating a focus on improving tribological behavior to enhance their practical utility. However, challenges persist due to limited insight into the tribological behavior of metal AM parts and the inherent anisotropic nature of the layer-by-layer manufacturing process [10,11]. Currently, AM surfaces exhibit significant roughness and irregularity, which contributes to increased coefficients of friction (COFs) and susceptibility to wear compared to traditionally manufactured parts [12,13].

Research on the tribological behavior of metal AM components is expanding, focusing on how AM technique choice, materials, process parameters, and post-processing impact mechanical properties, friction, and wear resistance [12]. Studies also investigate AM's potential in specialized applications, such as energy systems, medical implants, and self-lubricating coatings [14–16]. Recently, some of the authors provided an in-depth review [7] of the current research in the tribology of AM components, encompassing a total of 165 published articles. It was reported that fundamental research remains the primary focus, though there is an emerging trend toward applications in medical technology due to additive manufacturing's suitability for producing customized one-of-a-kind components. Most tribological studies center on metal materials, with stainless steel and titanium alloys as the primary subjects of investigation. Among AM processes, powder bed fusion techniques are the most utilized. The authors suggested that future trends in the tribology of AM components are likely to emphasize process optimization, functional integration, and advanced surface treatments, such as coating and post-processing. The latter is also the focus of a review by Shah et al. [13], who summarized the state of research in terms of post-AM chemical, mechanical or laser-based material removal, heat treatment, or hot isostatic pressing as well as laser shock and shot peening to enhance the surface topography and tribological behavior. As such, mechanical machining, such as grinding or polishing, is a widely used and cost-effective approach for reducing the roughness of AM surfaces [17,18]. One of the most effective laser-based techniques is laser polishing, which can significantly reduce surface roughness as well as enhance fatigue and wear resistance [19–21].

Although not only the material but also the AM process itself has a considerable influence on tribological behavior, most studies concentrate on optimizing individual AM processes rather than on a comparative analysis of the wear and friction behavior of different processes. Merley, Attar et al. [22] analyzed pure titanium samples produced by LPBF, laser-engineered net shaping (LENS), and WAAM to assess differences in mechanical properties and tribological behavior for medical applications. Li et al. [23] found no notable difference in wear resistance between Ti6Al4V samples manufactured by various LPBF processes or conventional methods, even at elevated temperatures. García--Hernández et al. [24] investigated the tribological behavior of SLM and FFF manufactured and polished samples made of 17-4 PH in comparison to hardened reference material in lubricated and dry pin-on-disc tribometer tests against alumina balls. In all cases, they were able to determine significantly reduced wear of the AM samples compared to the reference. MEX-AM processes are therefore also an interesting approach for the production of metal components, but different MEX-AM processes have not yet been extensively investigated and compared directly with LPBF processes in terms of tribological performance [7]. Further research could reveal its potential as a competitive alternative in AM tribology studies.

The material 17-4 PH is frequently used in applications requiring both corrosion resistance and good mechanical performance. However, process-induced porosity and defects can impair the corrosion resistance of additively manufactured components. Previous studies have linked corrosion susceptibility of AM 17-4 PH to process-related porosity and surface characteristics [25,26], while reported effects of AM processing on passivation behavior remain inconsistent [27,28]. Overall, the available data on corrosion resistance of AM 17-4 PH in chloride-containing environments remain scarce and difficult to compare.

To summarize, while numerous studies have explored the tribological characteristics of AM metal components, a significant research gap remains in directly comparing these characteristics across different AM techniques using a controlled set of materials to understand how different methods impact tribological behavior. Variability in surface characteristics, porosity, and microstructure between techniques can influence performance, yet comparative studies are scarce. Additionally, although metal extrusion AM processes show promise as an alternative approach, their tribological performance has yet to be evaluated comprehensively or compared with more established LPBF methods. To address this gap, the present experimental study systematically examines the tribological behavior of parts produced by LPBF and two MEX processes, assessing them under both dry and lubricated conditions with and without further post treatment. The objective is not to reproduce a specific tribological application, but to establish a controlled comparative framework that enables the assessment of process-dependent influences on friction, wear, and corrosion behavior. The selected tribological model contact is therefore intended to provide fundamental insight into process-structure-tribology relationships rather than application-specific performance data. Since each process has its own unique characteristics, which can sometimes vary greatly and are difficult to examine as individual factors without changing the process itself, we have deliberately opted for a holistic approach in which the differences in porosity, microstructure, and binder are considered intrinsic. This is done using the example of 17-4 PH stainless steel, a precipitation-hardening martensitic alloy, which is a preferred choice for applications requiring a combination of high strength, hardness, corrosion and wear resistance in aerospace, marine, and industrial applications. The alloy was deliberately selected because it is widely used in such applications while being compatible with all investigated additive manufacturing routes. Consequently, the objective of this work is not to compare different steel grades, but to isolate and assess the influence of the manufacturing route on tribological and corrosion performance within a single alloy system. 17-4 PH is known for its excellent mechanical performance, suitability for post-processing, and can be hardened to various degrees, allowing the assessment of how AM methods impact hardness and wear resistance in high-strength materials. This versatility also aids in exploring the effects of AM surface characteristics on friction and wear, offering insights into how different AM processes might optimize this alloy for specific tribological applications. By analyzing surface morphology, microstructure, corrosion resistance, chemical composition, and friction and wear mechanisms across these 3 a.m. methods, this research ultimately aims to establish a framework for selecting AM processes based on specific tribological needs. At the same time, a statistical approach for comparing additively manufactured technical surfaces is presented for the first time to understand their complex influence on tribological behavior.

2. Materials and methods

2.1. Material

The stainless steel 17-4 PH (1.4542/X5CrNiCuNb16-4 according to DIN EN 10088-3, AISI 630 according to ASTM F899) was examined in three different AM processes in addition to a conventionally manufactured reference. In addition to LPBF two material extrusion AM processes were investigated in which a filament highly filled with metal powder is first printed and the resulting green parts are then debinded and sintered. The main advantages of these MEX processes are the significantly reduced investment costs as well as the simple and

harmless filament compared to metal powder. Subsequent heat treatment was deliberately not carried out to specifically investigate the influence of the actual AM processes. The resulting, process-dependent differences in hardness and microstructure are therefore a certain limitation that must be considered.

In all cases, round, fully filled shims with a height of 5 mm and a diameter of 30 mm were used as test specimens. As a conventional reference, wrought (hot-rolled) 17-4 PH stainless steel bar stock in precipitation-hardened condition H1025 (aging at 550 °C) was used. The material was cut into 5 mm thick specimens and subsequently ground. The measured hardness as well as the tensile strength (1220 MPa from manufacturing information) are consistent with this heat treatment.

The LPBF test specimens were fabricated from 17 to 4 PH powder (CL 92 PH, Colibrium Additive, earlier General Electric, USA) with a particle size of 45-55 µm processed by laser powder bed fusion (LPBF) using a MLab 200R unit (General Electric, USA) equipped with a fiber laser and a pair of galvos scanning mirrors, and f-theta lens, as well as two stepper motor-controlled platform stages. Four specimens per batch were printed in a two-by-two arrangement on a stainless-steel build plate using a layer height of 0.015 mm, a laser power of 180 W, a speed of 200 mm/s, and an interlayer rotation scanning pattern with a hatch spacing of 0.070 mm, resulting in an energy density of 857 J/mm^3. After printing under argon atmosphere (oxygen content < 0.3%), the samples were separated from the build plate by wire-cutting (Jiangsu Sammlite Machinery, China).

In the first MEX process the 17-4PHv2 filament from Markforged (USA) was used. As Markforged advertises its closed process chain as atomic diffusion additive manufacturing, these specimens are referred to below as ADAM. Alternatively, and due to its easy accessibility and use on consumer MEX machines, the Ultrafuse® 17-4 PH filament from BASF (Germany), further referred to as MEAM, was investigated. Both processes consist of the three steps of MEX, printing, debinding and sintering, for the latter the specimens from ADAM and MEAM were sintered in flatwise orientation, the difference between both routes are described in the following.

The ADAM process is self-contained and is adapted to the company's own filament and the associated equipment. The wax-based filament was first printed on the Metal X printer with a layer height of 125 µm and a nozzle diameter of 0.4 mm. The samples were then debinded and dried in the Wash-1. The final sintering process took place under a protective gas atmosphere (Ar, Ar+ 2.93% H_2) in the Sinter-1. Since it is a closed system with material dependent debinding and sinter parameters predefined for the Markforged materials, no information about the temperatures, holding times, heating or cooling rates is provided.

The BASF filament (MEAM) contains polyoxymethylene (POM) as a polymeric binder and was printed on a UltiMaker S5 (UltiMaker, Netherlands) with Metal Expansion Kit with a layer height of 0.150 mm and a nozzle diameter of 0.4 mm. The finished green components were then chemically debinded using the established industrial CataMold® process. In this process, nitric acid (HNO_3) is injected into a gas-tight oven at a temperature between 100 °C and 140 °C, dissolving the POM binder starting from the edge zones. This decomposition process runs inwards at a rate of 1-2 mm per hour. The subsequent sintering process included a holding stage at 600 °C to remove the remaining binder-backbone. Subsequently the parts were sintered at 1360 °C under H_2-atmosphere for 30 min.

The chemical composition of the metal powders and reference materials according to the datasheets of the manufactures is shown in Table 1.

As the untreated AM surfaces do not appear to be suitable for most tribological applications, the subsequently polished surfaces in addition to the untreated surfaces were examined. The samples were polished to $R_a < 0.04$ µm with increasingly finer grain sizes (mesh 220, 500, 1000, 2000, 4000) on a RotoPol-31 (Struers, Denmark). As a special feature of the SLM process, subsequent laser polishing was applied. In this process, the laser passed over the top layer again three times with a power of 180 W, a speed of 200 mm/s directly after the actual printing process to re-melt and smoothen the material. The laser polishing was considered a process-compatible post-treatment rather than an external modification introducing systematic bias relative to the other AM routes, for which an equivalent in-process laser remelting step is not technically applicable.

2.2. Physical and mechanical properties and surface analysis

To record the differences in porosity resulting from the AM processes, bulk density measurements were carried out according to Archimedes' principle, i.e weighing specimens in water and air, using a precision balance (TGD 50-3C, Kern, Germany). The hardness was determined using Rockwell hardness testing (HRC, DuraJet10G5, ZwickRoell, Germany) according to DIN EN ISO 6508-1 [29]. Microhardness measurements (Fischerscope HM 2000, Helmut Fischer, Germany) were carried out in accordance with DIN EN ISO 14577-1 [30] to determine the microscopic mechanical properties independently of the porosity in the areas with solid material. The test force was set at 200 mN after preliminary tests. The surfaces were recorded with light microscopy (Metallux I, Leica, Germany and VK-X3100, Keyence, Japan) for qualitative evaluation. In addition, the height profiles of the surfaces were recorded using laser scanning microscopy (LSM, VK-X3100, Keyence, Japan). Standard roughness characterization alone is often insufficient for AM surfaces because their multiscale topography cannot be adequately described by a conventional roughness–waviness separation. To obtain statistically meaningful information about the complex surface topography, the surfaces were methodically analyzed as follows. First, four primary profiles per sample were recorded, each of which was composed of four images (20× magnification) in the LSM. As the surfaces of the AM samples have a strongly multiscale character, the height data of the primary profile was used for the evaluation without filtering. 24 surface parameters standardized according to ISO 25178 [31] were examined using the VK-X 3000 MultiFileAnalyzer software (Keyence, version 3.3.1.85). The standardized surface parameters were statistically evaluated to identify significant differences between the manufacturing processes. One-way ANOVA and Kruskal-Wallis tests with Bonferroni correction ($p = 0.05$) were applied, followed by post-hoc analyses (two-sided *t*-test for unpaired samples and non-parametric Wilcoxon rank sum test) including the reference material. In addition, principal component analysis (PCA, Python, sklearn 1.6) was performed to reduce the multidimensional parameter space and enable a comparative assessment of similarities and differences between the investigated surfaces.

2.3. Tribological characterization

The tribological behavior of the AM samples was analyzed using

Table 1
Chemical composition of the raw material as informed by the manufacturers in weight-%.

Material	Fe	C	Cr	Ni	Cu	Mn	Mo	Nb	Si	P	S
Reference	Rest	<0.07	15.0-17.0	3.0-5.0	3.0-5.0	<1.5	<0.6	<0.45	<0.70	<0.04	<0.015
ADAM	Rest	<0.07	15.0-17.5	3.0-5.0	3.0-5.0	<1.0	n.a.	0.15-0.45	<1.0	<0.04	n.a.
LPBF	Rest	<0.07	15.0-17.5	3.0-5.0	3.0-5.0	<1.0	n.a.	n.a.	<1.0	<0.04	<0.030
MEAM	Rest	<0.07	15.0-17.5	3.0-5.0	3.0-5.0	<1.0	n.a.	0.15-0.45	<1.0	n.a.	n.a.

tribometer tests (MT1, LSCAD, Germany) in ball-on-disc configuration, unlubricated (setup 1), e.g. technically dry, and lubricated (setup 2). The selected contact pressures were chosen to represent highly loaded concentrated contacts, which are typical for bearing-like interfaces, pumps, valves, and comparable machine elements. The selected sliding speed favors boundary and mixed lubrication conditions, thereby increasing the influence of surface topography, porosity, and microstructure on the tribological response. According to elastohydrodynamic lubrication (EHL) estimations and experimental experience with similar tribological systems, setup 2 is clearly in the mixed lubrication regime. The objective of the present study was not to reproduce a specific tribological component but to establish a reproducible loading condition that enables a comparative assessment of the investigated additive manufacturing routes. The selected ball-on-disc configuration represents a well-established tribological model system that allows fundamental friction and wear mechanisms to be studied under controlled conditions. In addition to the lubricated tests, dry sliding was also included to distinguish dominant wear mechanisms and expand the range of application-relevant load scenarios, especially for corrosion-prone components such as pumps, valves, or maritime systems. The laser-polished LPBF samples were only analyzed in setup 1. In the tribometer used, the normal force is applied via a fixed weight, while the frictional force is recorded tangentially to the friction track via a load cell on the cantilever of the test rig. The uncertainty of the force measurement was determined experimentally to be $U = 30$ mN ($k = 2$). The test conditions are summarized in Table 2. All tribological tests were conducted in triplicate, i.e., three repeated independent runs. The reported friction and wear values therefore represent statistically evaluated results. This is particularly important for additively manufactured materials, where process-related variations may lead to increased scatter in tribological performance.

In addition to measuring the friction during the tests, the wear of the base and counter body was also determined. The wear diameter on the ball was recorded using an optical microscope and the wear volume was estimated from the measured scar diameter assuming a spherical wear cap with a flat wear scar. This approach is commonly used in tribological investigations but may introduce a systematic bias, particularly for small wear scars where deviations from the assumed geometry become more relevant. The resulting wear volumes should therefore be interpreted primarily as comparative values. Future studies should preferably employ 3D optical measurements for a more accurate determination of ball wear volume. The wear of the flat specimens was determined volumetrically using 3D laser scanning microscopy (LSM). For this purpose, averaged wear profiles were recorded at four points of each wear track offset by 90° and the cross-sectional wear area below the unworn reference plane was determined in the MultiFileAnalyzer software. The volume was calculated using the measured diameter of the wear track and the wear area. An exact estimation of the measurement uncertainty is not possible due to a lack of standards. Nevertheless, the signal-to-noise ratio at the selected magnification in the LSM was sufficiently high and the uncertainty associated with the optical determination of the wear scar diameter is considered small compared to the observed differences between materials.

Table 2
Test conditions for Setup 1 (dry) and Setup 2 (lubricated).

	Setup 1 (dry)	Setup 2 (lubricated)
Base body	17-4 PH specimen with height $h = 5$ mm and ∅30 mm Reference, ADAM, MEAM, SLM	
Counter body	100Cr6 (1.3505) balls with ∅4.000 mm, grade G10, DIN 5401, Ra ≤ 0.02 µm, hardness ≥ 61 HRC	
Base body surface	Untreated and polished to $R_a < 0.04$ µm SLM: laser-polished	Untreated and polished to $R_a < 0.04$ µm
Lubricant	None	10 µl PAO-40
Normal force F_n	5 N	10 N
Initial Hertzian pressure p_h	1.47 GPa	1.85 GPa
Sliding speed u	0.1 m/s	
Track radius r	10 mm	
Maximum sliding distance w	1000 m	
Relative humidity range	37-48%	41-53%
Temperature range	20.7-22.6 °C	20.8-22.8 °C

2.4. Metallographic and chemical characterization

For a more precise analysis of the material, the samples were destructively tested following the tribological tests. To do this, they were first cut in the middle on a cutting machine (Brillant 240, QATM, Germany) and then embedded in epoxy resin (EpoFix, Struers, Denmark). Subsequently, the samples were automatically surface-ground (mesh 220, 500, 1200) on a metallographic polishing machine (Pabo Pol 30, Struers, Germany) and then polished (suspension 9 µm, 3 µm, 1 µm). The resulting sections were examined by light microscopy for porosity and macrostructure. For the metallographic analysis, a polishing with colloidal silicon oxide suspension was carried out. The samples were then etched with V2A pickling solution (100 ml H_2O, 100 ml HCl, 10 ml HNO_3, 0.3 ml Vogel's Sparbeize) for 15 s and then analyzed using light and laser microscopy.

The elemental composition of the materials was measured by glow discharge optical emission spectroscopy (GD-OES) using Spectruma 750HR (Spectruma, Germany) in Ar-gas determining bulk composition at three points and depth profile analysis (DPA). For the DPA, the as-fabricated samples were measured to account for the process specific surface. The polished surfaces and the wear tracks tests were also analyzed using SEM (Zeiss Ultra plus, Carl Zeiss, Oberkochen, Germany) with Inlens-SE-Detector and Chamber-SE-Detector. The elemental distribution was determined using EDS (Thermo Fisher Scientific NS7, Themo Fisher Scientific, Waltham, USA) at an acceleration voltage of 20 kV. In addition, Raman spectroscopic investigations of the wear tracks on the polished samples were carried out using an i-Raman Plus (Metrohm, Filderstadt, Germany). The spectra were recorded using a 50-fold magnification with a wavelength of 532 nm and 30 mW laser power. The raw data was smoothed using a Savitzky–Golay filter (3rd order polynomial) and then subjected to asymmetric least squares baseline correction (ASLS) to remove fluorescence background. Spectral processing was performed using the Python library RamanSPy. After baseline correction, the spectra were normalized for better comparability.

2.5. Electrochemical characterization

The electrochemical response was determined in a 3.5 wt% NaCl (0.6 mol) using a three-electrode arrangement and exposing 1 cm^2 of the working electrode, i.e., the test sample. The reference electrode and counter electrode were Ag|AgCl and graphite rod, respectively. On the as-made samples, cathodic and anodic polarizations were conducted at the scan rate of 0.5 mV/s after stabilization of the Open Circuit Potential (OCP), cathodic one from OCP to −0.5 V vs OCP, and anodic one from OCP to +1 V vs OCP. In addition, cyclic polarization was conducted on mechanically polished samples. First, OCP was recorded for 1 h followed by anodic polarization from −0.3 V vs OCP and reverting the direction to cathodic after reaching the current density target.

3. Results and discussion

3.1. Physical and mechanical characterization

The resulting bulk density of the sintered samples and the macroscopic Rockwell hardness are summed up in Fig. 1(a) and (b). Compared to the reference, all additively manufactured samples showed a lower bulk density, although the difference in LPBF was not significant (ns).

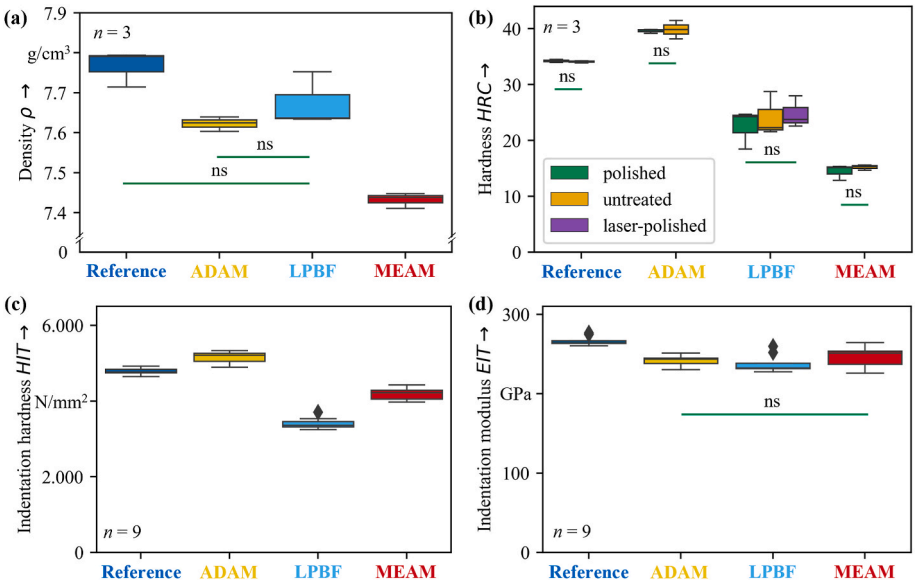


Fig. 1. Boxplot of Bulk density (a) and macroscopic Rockwell hardness (b) as well as microscopic indentation hardness (c) and indentation modulus (d) of the test specimens depending on the manufacturing process. Significance levels (ns = not significant) from two-sided *t*-test for unpaired samples und non-parametric Wilcoxon rank sum test with $p = 0.05$. Outlier are marked with diamonds.

ADAM and especially MEAM showed increased porosity due to the debinding and sintering process, which is reflected in the lower bulk density. The bulk density of the MEAM samples is similar to Ref. [32] and also [6], where a slightly higher density of 7.47 g/cm^3 was determined for samples printed from metal injection molding feedstock Catamold® 17-4 PH F. The ADAM samples achieved a significantly higher bulk density compared to samples in Ref. [33]. The high relative density (>97%) of the LPBF samples is comparable to typical literature values [34,35].

To determine the effect of the surface topography on macroscopic hardness, the tests were carried out on polished and untreated surfaces. The Rockwell hardness was not influenced by the surface treatment for each individual material, as expected, which is due to the relatively greater penetration depth of the indenter. On the other hand, Rockwell hardness differed substantially between the different manufacturing processes. The hardness of the ADAM samples was higher than for reference, while LPBF and MEAM samples showed significantly lower hardness. In addition to the clear influence of the different phases and grain sizes formed, this is mainly due to the very porous structure of the MEAM samples. At the micro level, reference, ADAM and LPBF samples showed similar relative behavior regarding indentation hardness (c) compared to the macroscopic hardness, as porosity has a minor influence here. With MEAM, however, this was significantly higher than with LPBF, which shows the clear effect of the porous structure. In the case of MEAM, the measurement had to be repeated at three points in the solid material because there were areas with very low hardness. Similar to the preliminary tests, these areas occurred at approximately 20–25% of the measurement points. We assume that these are areas where binder residues were present on the surface. This assumption is described in more detail in the metallographic analysis. The indentation modulus (d) was below the reference for all AM techniques, but no significant differences were discernible between the processes.

3.2. Surface topography

Representative surfaces resulting from the different manufacturing processes used and their height profile untreated and polished are depicted in Fig. 3. The ground (i) reference showed the typical grinding marks of conventional production, while in the polished case (a) only the smallest scratches could be seen, which are close to the dissolvability of the LSM. The as-build ADAM (j) and MEAM (l) surfaces showed the typical path patterns of MEX processes. In this case, the surface fabricated by ADAM was finer, and the individual paths merged smoothly into one another, whereas in MEAM fabricated surfaces they were much more pronounced. After polishing, the process-related differences became even greater. ADAM (b) surfaces were very smooth with micropores, which occasionally showed macropores. As these predominantly occurred in the cross pattern with a distance between the path widths, it can be concluded that the pores result from the intersections of the intermediate path areas between two layers. With MEAM (d), on the other hand, no path-related pores were recognizable, but the surface had significantly larger pores, which is also reflected in the lower density (see Fig. 1). The unpolished LPBF samples (k) showed the typical melt pool marks with solidification waves as well as isolated particles resulting from melt splashes. The laser polishing process (q) melts the surface again and the surface, including previously existing particles, is smoothed to a much more homogeneous finish. By polishing (c) a closed surface without recognizable pores was created. In contrast to the MEX process, however, there were occasionally larger defects near the surface.

Since individual surface topography cannot be used to draw conclusions about tribological behavior and the surfaces are subject to strong process-related fluctuations, especially in AM, a statistical approach is chosen as described in 2.2. to evaluate the similarity of the surfaces and to be able to derive correlations. The results of the PCA for the polished (a) and untreated (b) surfaces are shown in Fig. 4. Polished, the different processes were relatively close together, the individual outliers in LPBF occur in the randomly selected surface areas where larger defects have occurred, such as in Fig. 2 (c). From a process perspective, the fluctuations within one group are of particular interest. For ADAM, this was quite comparable to the reference, which indicates reproducible process control with homogeneous surface porosity. With MEAM, the fluctuations were somewhat greater with isolated outliers. These indicate a somewhat more inhomogeneous porosity. The LPBF surfaces without major defects were also very close together. In the untreated (b) state, all AM processes deviated more strongly from the reference and almost three quarters of the variance can be explained by the first two principal components PC1 and PC2. The scatter of the reference was low, as is to be expected for conventional production. With ADAM, the variance was not much greater, and the process is

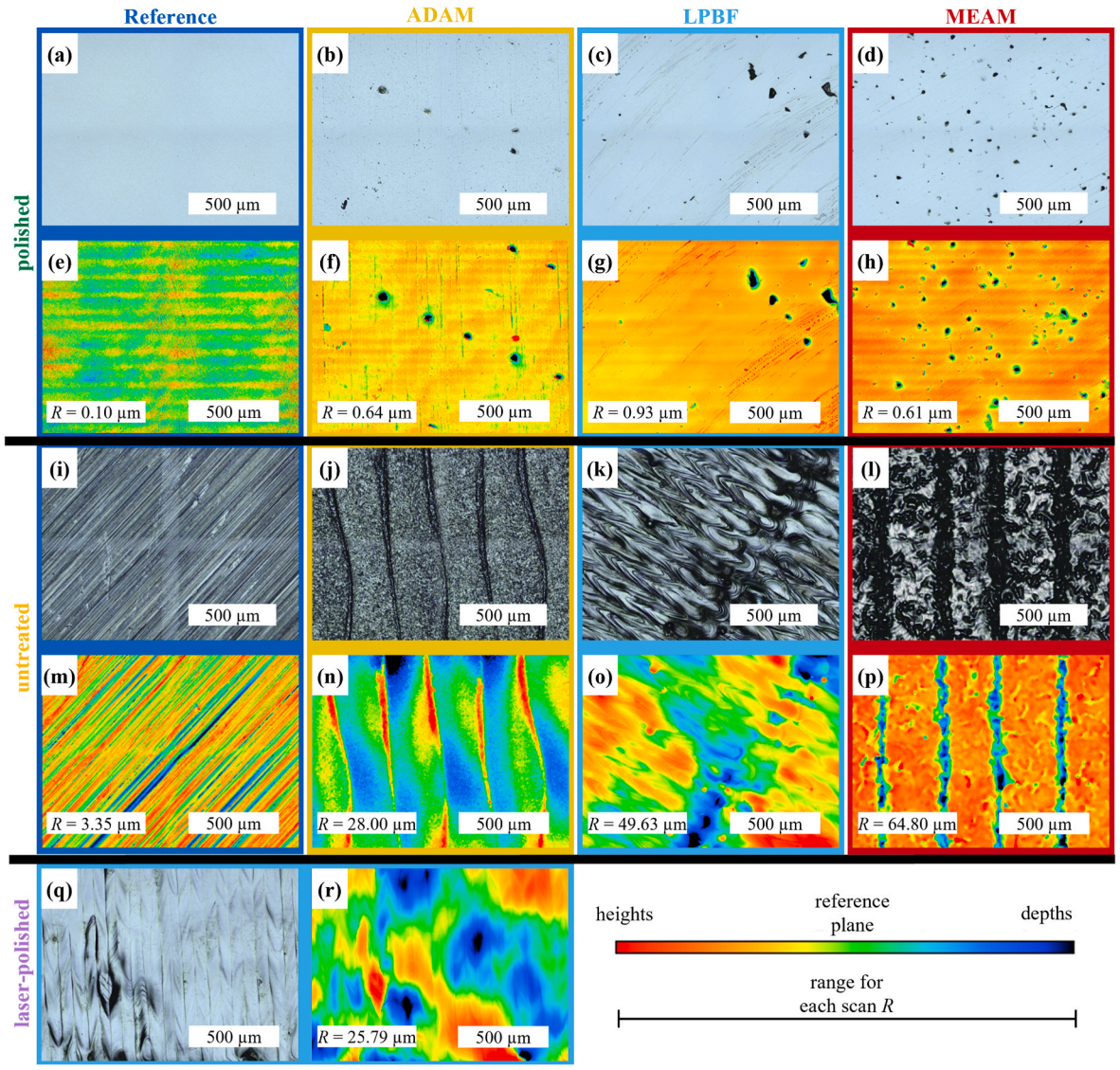


Fig. 2. Process-dependent surfaces polished ((a)-(h)) and untreated ((i)-(p)) with light (e.g. (a)) and laser microscopic (e.g. (e)) images. The additionally laser-polished surfaces from the LPBF are shown in (q) and (r). Due to the very different scales, the LSM profiles are normalized to the respective minima and maxima and the range is given. The horizontal line traces of the polished surfaces are merely measurement artifacts due to the very low surface roughness in the order of magnitude of the measurement uncertainty of the LSM.

closest to the reference. ADAM therefore has the most reproducible surfaces in the untreated state in terms of process technology. With MEAM, two groups could be clearly distinguished. In addition to the surface areas with a normal path structure (see (h) above), there were areas in which these are barely recognizable (see (h) below). The latter deviate strongly from all other samples in PC2, as they have a very irregular and speckled surface. We attribute these two protruding surfaces to deviations in the process, such as an inhomogeneous material flow or a printing platform that is not exactly leveled. The large scattering of the LPBF samples is because the melt paths are more irregular than the paths of the MEX processes and at the same time areas with overlapping paths occur due to the scanning strategy (see Fig. 2 (k)).

The statistical procedure made it possible to identify five standard parameters for the polished state in which the 3 a.m. processes differed significantly. In this case, it is interesting to note that the ADAM samples differed from LPBF and MEAM primarily in the profile peaks. The higher material content of the peaks S_{mr1} (c), the higher peak density S_{pd} (d) and the higher peak curvature S_{pc} (e) indicate that more peaks emerged from the fine-pored surface structure after polishing, which were also sharper. For dry tribological contacts, one can therefore assume rather unfavorable behavior. The skewness S_{sk} (f) shows that the material distribution of ADAM was generally symmetrical to the middle plane and similar to reference. For LPBF and MEAM, the material distribution was clearly shifted above the middle plane. The significantly higher maximum valley depth S_v (g) is due to the defects in LPBF surfaces and the large and shallow pores in MEAM surfaces. These individual valleys could serve as a lubricant reservoir in the lubricated contact and keep the lubricant in the contact.

Untreated, the surfaces were much more different. Apart from S_{al}, S_{pd}, S_{dr}, S_{ku}, S_{td} and S_{tr}, all standard parameters differed significantly. Therefore, for example, some parameters were selected with particularly high f-values from the ANOVA or H-values from the Kruskal-Wallis test. The very different profile distribution S_{sk} (h) is particularly striking. While LPBF fabricated surfaces had a symmetrical profile, the material content for ADAM surfaces was predominantly below the middle level and for MEAM surfaces above, which appears to be tribologically favorable. The maximum depth of the valleys S_v (j) was significantly greater for LPBF and MEAM surfaces, whereby the distribution into two groups for LPBF can be explained by the laser polishing and for MEAM by the different surfaces according to (h). The peak density S_{pd} (k) was

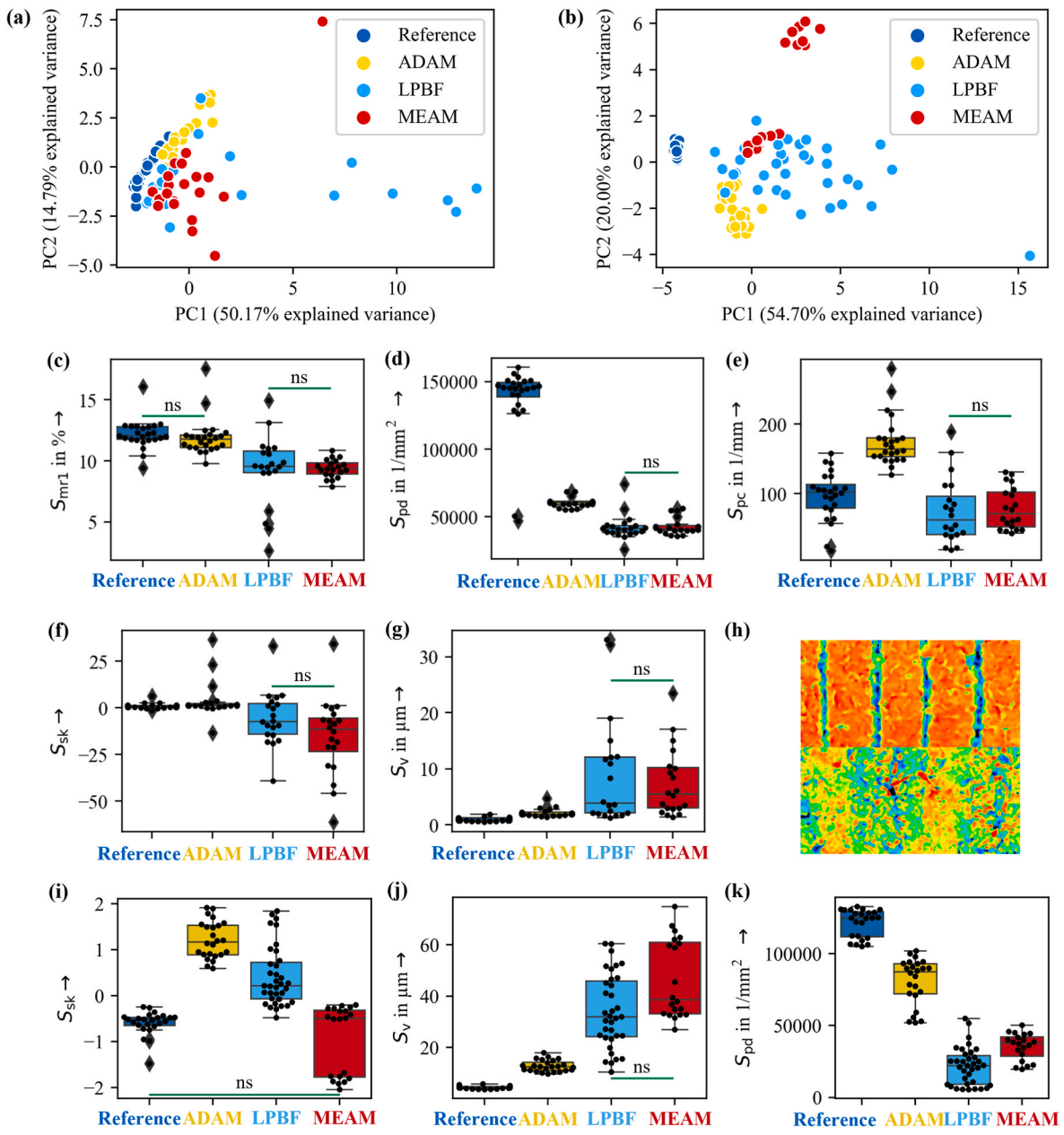


Fig. 3. Statistical surface analysis: PCA of the polished (a) and the untreated or laser polished (b) surfaces, significantly different parameters S_{mr1} (c), S_{pd} (d), S_{pc} (e), S_{sk} (f) and S_v (g) of the polished surfaces, Process-related profile differences of untreated surfaces in the MEAM process (h), Selected significantly different parameters S_{sk} (i), S_v (j) and S_{pd} (k) of the untreated surfaces. Significance levels (ns = not significant) from two-sided *t*-test for unpaired samples und non-parametric Wilcoxon rank sum test with $p = 0.05$ corrected using the Bonferroni method with $k = 24$.

also significantly greater for ADAM surfaces in the untreated state than for LPBF and MEAM surfaces.

3.3. Metallographic and chemical characterization and analysis of process-related differences

The elemental composition of the samples determined by the GDOES bulk analysis, i.e. within a depth of up to approx. 200 µm below the surface, is summarized in Table 3. Composition of all samples was within the specification of the 17-4 PH grade and within the specification of the powder used for the fabrication (Table 1).

The depth profiles of the elemental composition of the as-fabricated samples are summarized in Fig. 4, displaying the relative content of iron, oxygen and carbon. All samples showed a layer of surface oxides and carbon contamination. In comparison to the reference samples, all the AM-materials show a deeper extension of the oxide consistent with the presence of pores. In the case of the ADAM and MEAM samples, there was a notable near surface oxidation of approx. 50 and 100 nm, respectively on the top surface and the profile of carbon is indicative of undercutting shape of surface pores, i.e. pores with an opening to the surface being smaller than the underlaying pore diameter.

Representative light microscope images of the microsections resulting from the individual AM processes are shown in Fig. 5. As expected, no defects were visible in the polished reference (a); after etching (e,i), manganese sulfides were clearly visible, which were present in the rolling direction of the base material. The microstructure itself was fine-grained and heterogeneous with a predominantly martensitic phase. The sections of the wear tracks (see (m)) were also examined to detect possible changes in the microstructure due to tribological contact. However, structural changes were not detected in any of the processes

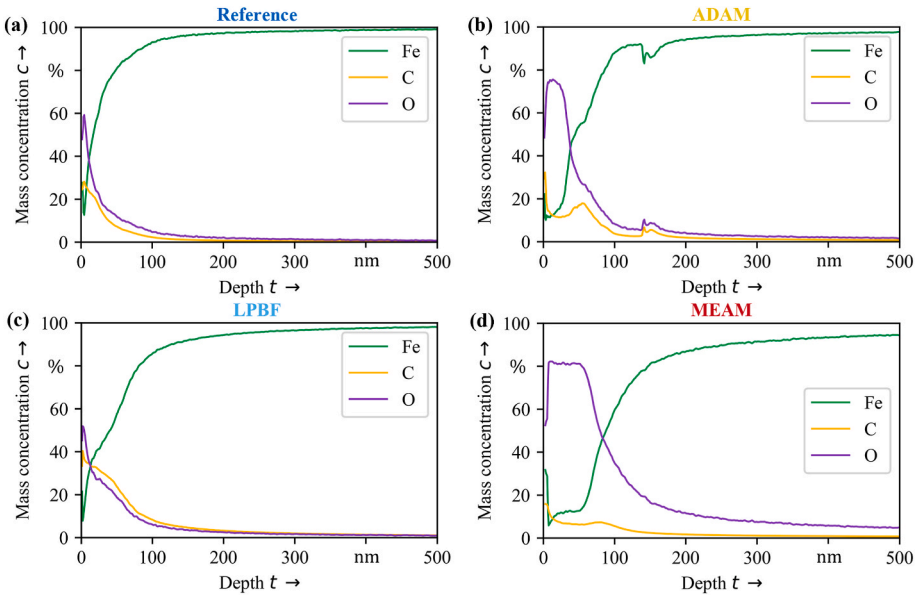


Fig. 4. Relative content of iron, oxygen and carbon versus depth for (a) Reference, (b), ADAM, (c) LPBF, and (d) MEAM as obtained by GDOES.

Table 3
Chemical composition of the manufactured specimen in weight-% for $n = 3$ with standard deviation.

Material	Reference	Std. Dev.	ADAM	Std. Dev.	LPBF	Std. Dev.	MEAM	Std. Dev.
Fe	76.100	0.031	74.698	0.300	74.750	0.097	75.330	0.024
C	0.010	0.000	0.068	0.000	n.d.	n.d.	n.d.	n.d.
Cr	14.822	0.017	16.183	0.100	15.444	0.007	15.891	0.016
Ni	4.622	0.021	4.322	0.018	4.804	0.023	4.432	0.010
Cu	2.920	0.009	3.833	0.016	3.632	0.114	3.414	0.012
Mn	0.678	0.001	0.139	0.002	0.452	0.002	0.228	0.001
Mo	0.143	0.000	0.024	0.000	0.123	0.001	0.001	0.000
Co	0.063	0.001	0.032	0.000	0.033	0.001	0.020	0.000
V	0.028	0.001	0.025	0.001	0.021	0.001	0.010	0.000
W	0.074	0.001	0.068	0.001	0.073	0.001	0.069	0.001
Nb	0.224	0.001	0.255	0.002	0.282	0.002	0.248	0.001
Zr	0.026	0.001	0.024	0.001	0.026	0.001	0.026	0.000
Si	0.265	0.001	0.310	0.003	0.327	0.001	0.319	0.001
P	0.018	0.000	0.010	0.000	0.016	0.000	0.006	0.000
S	0.005	0.000	0.007	0.000	0.010	0.000	0.004	0.000
Al	0.004	0.000	0.004	0.000	0.005	0.000	0.004	0.000

n.d. – not detected (below detection limit).

examined.

The microstructure of the ADAM samples was homogeneously fine-pored (b). Due to the sintering process, the microstructure was independent of the printing direction. A partially oriented structure as in Ref. [36] could not be observed and the original powder particles and the melt phase transitions can be partially recognized. At higher magnification, isolated larger pores (see (j)) and residues in the pores (n) became visible. These are presumably due to binder residues. In the etched state, the predominantly martensitic structure became visible. This matches the high hardness and the findings described in Ref. [37]. In addition, defects resulting from the non-ideal material deposition between the paths and layers during printing came up. Similar defects have already been reported in Ref. [37]. Since these defects only appeared after etching, we assume that binder residues were also deposited in these areas during the process. In Ref. [38], similar defects were also found for the Bound Metal Deposition Additive Manufacturing.

The MEAM samples had a rather coarse-pored microstructure, whereby the material is significantly denser in the edge areas (d). Based on the edge layer thickness, it can be concluded that the wall and surface layers exhibit improved process control compared to the infill area. In the etched state (h), a very coarse-grained martensitic microstructure was observed, which was reported in Ref. [39] for similar sintering temperatures. In the surface regions (l), the grains were predominantly oriented in the surface direction. We attribute this to the cooling process, as there was no preferential orientation in the center region of the samples. Overall, the microstructure occurring with MEAM was like alternative MEX processes investigated [40]. The etching process revealed significantly larger pores (p), which were predominantly oriented along the layer boundaries (h). The pore distribution is similar to that described in Ref. [39]. We assume that these are because of now dissolved POM binder residues. The pores found also correlate qualitatively with the microhardness measurements, in which significantly lower values were determined in approximately 20-25% of the measurement points. In contrast to the two MEX processes, hardly any pores became visible in the LPBF samples. However, there were always isolated defects, especially near the surface, in the form of larger and smaller pores (e.g. (o)), which may be possible due to lack of fusion (large pores) and keyhole effects (small pores). Depending on the process parameters used, this appearance is typical [35]. In the etched state, the complex directional columnar martensitic structure parallel to the build direction became visible, similar as described in Ref. [41]. As described in Ref. [34], larger cracks (k) occurred along the melt pool lines. In contrast to the MEX processes, however, no new pores were

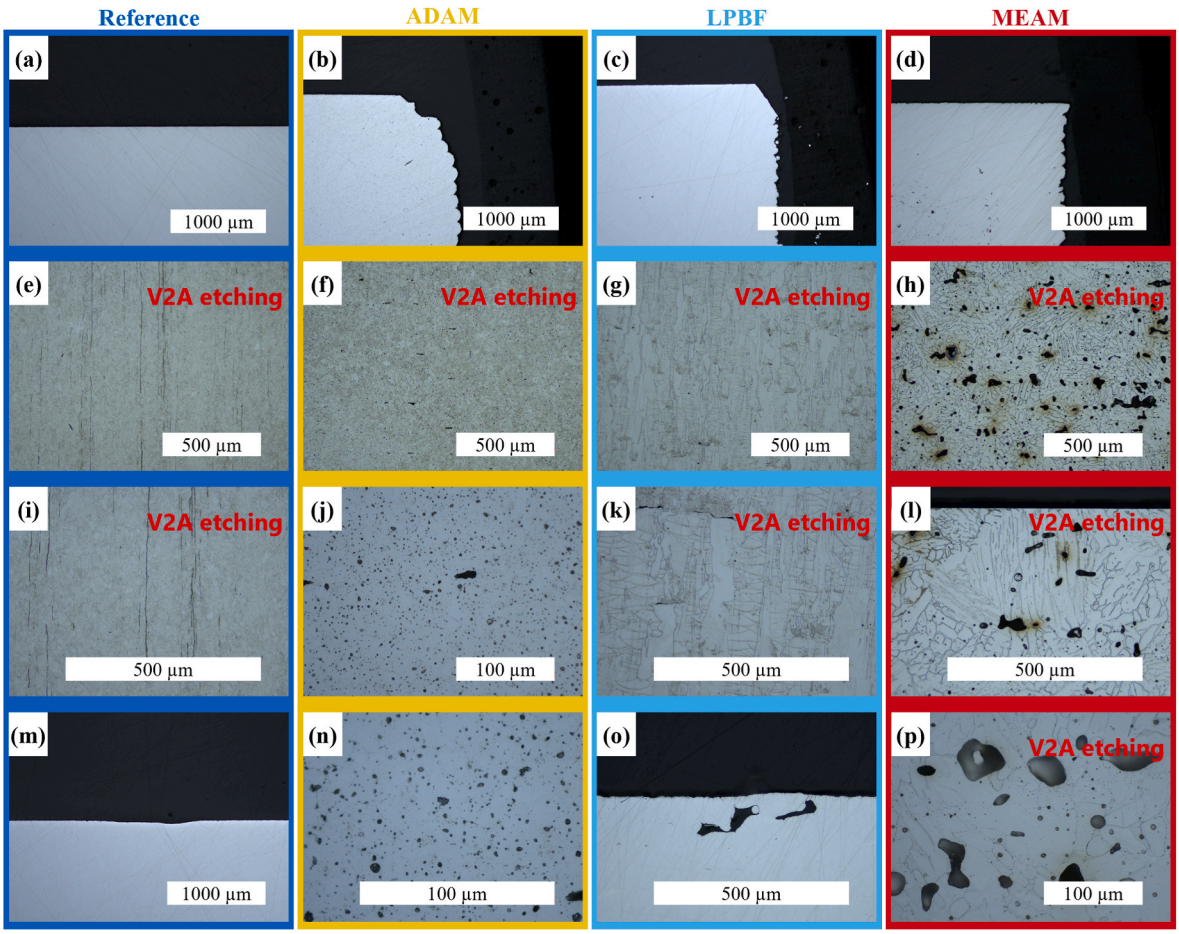


Fig. 5. Metallographic sections of the individual processes before (a, b, c, d, j, m, n and o) and after (e, f, g, h, i, k, l, p, marked) etching using V2A pickling solution at different magnifications where etching reveals the removed binder residues.

exposed as the LPBF process does not require an additional binder.

SEM images of the polished surfaces as well as of wear tracks with typical signs of wear and selected EDS mappings of near surface areas are displayed in Fig. 6. Noticeable differences were only found in the C and O distributions; all other elements were homogeneously distributed with proportions as already determined by the GDOES bulk analysis. The polished surfaces of reference (m), ADAM (n) and LPBF (o) showed no conspicuous carbon distributions, whereas MEAM (p) showed clearly recognizable local carbon deposits. These indicate residues from pyrolyzed binder. Overall, the C mass fraction in the binder-based ADAM and MEAM processes is significantly higher at 6.2% and 7.3% than in reference and LPBF processes at 2.5% and 2.8% respectively. With ADAM, however, this could not be dissolved locally. ADAM (f) and MEAM (h) also showed high local C concentrations in the wear track. As expected, oxidation in the dry test was locally distributed in reference, ADAM and MEAM, as shown in (e) for reference. In contrast, the strong oxidation in the wear track of LPBF (g) was conspicuous.

3.4. Tribological behavior in unlubricated and lubricated sliding contact

The results of the tribometer tests are summarized in Fig. 7, including representative coefficient-of-friction curves from the first repetition of each test condition. These curves provide an impression of the friction evolution during sliding but are not intended for a statistical comparison of transient friction behavior. In tribological analysis, the evaluation focuses on the previously defined mean coefficient of friction and wear volumes to ensure a robust and reproducible comparison between the manufacturing processes. Representative friction curves are additionally provided to illustrate the friction evolution during the tests. As is often observed in highly stressed tribological systems, the friction behavior showed substantial fluctuations over time. Under dry conditions (Fig. 7g), some tests exhibited drops in friction, which may indicate the formation of tribologically active surface layers or transient lubricating effects caused by residual binder. In the lubricated tests (Fig. 7h), recurring transitions between different lubrication regimes were observed. However, these characteristics were generally not reproduced consistently across all repetitions and therefore cannot be interpreted with sufficient statistical confidence. Consequently, the discussion focuses primarily on mean friction, wear, and post-test characterization results. The only consistently observed exception was the lubricated ADAM condition, which maintained stable low-friction behavior throughout the tests. The in-depth analysis of the wear patterns and the Raman analysis of the wear tracks on the polished samples are summarized in Fig. 8. In the dry tests on the polished surfaces, the ADAM samples were characterized with a highly significant increase in friction (Fig. 7a) compared to reference. The wear (Fig. 7c) was also significantly increased there, while the counter body, i.e. ball, wear was in a similar range. This contradicts the expectation that the ADAM sample with the highest hardness is also the most resistant to wear. We assume that the unfavorable tribological behavior in dry contact with the surface shape can be explained by many sharp protruding peaks shown in the surface analysis, which fail after a short time and then lead to third-body-wear. The SEM micrographs (Fig. 8n) also show an increased number of abrasive particles, which point to the same conclusion.

LPBF and MEAM samples exhibited a rather inconspicuous behavior compared to the reference. The MEAM samples tended to show the

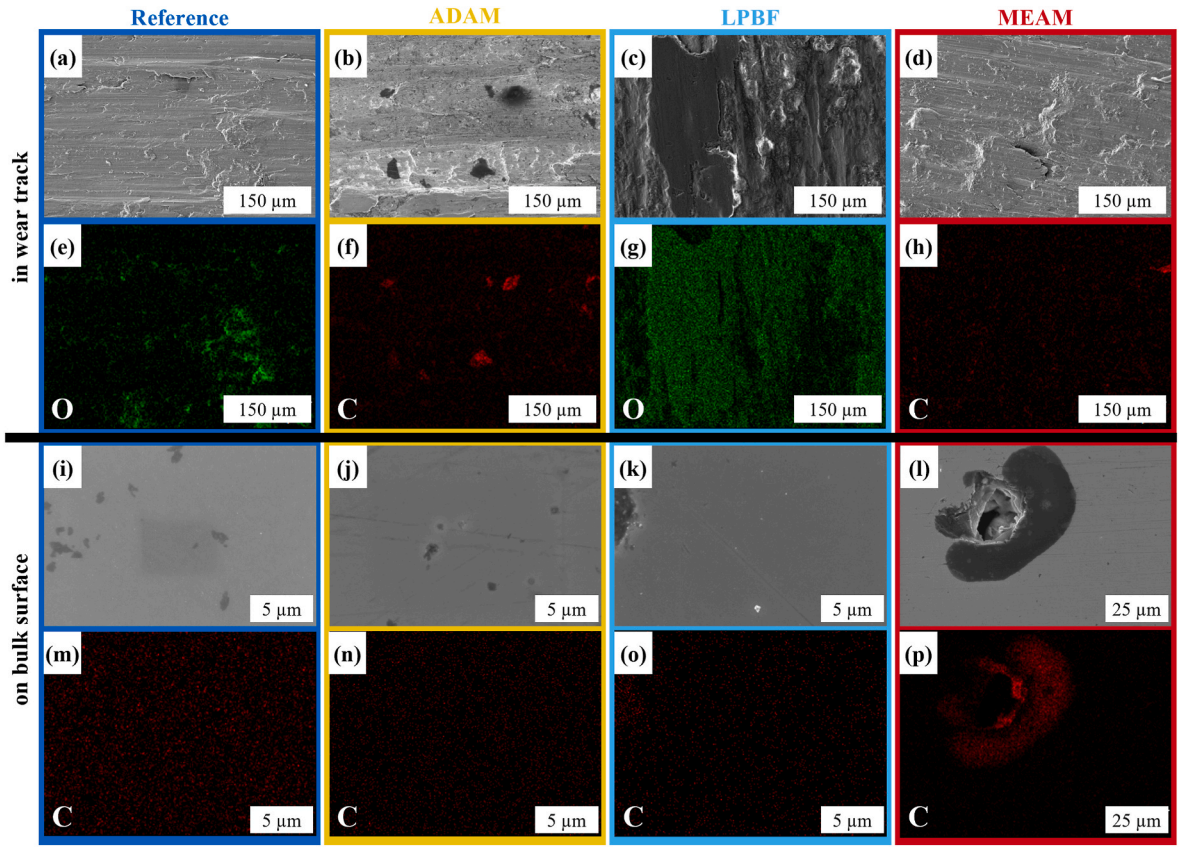


Fig. 6. Representative SEM micrographs of the wear track (a, b, c, d) with corresponding EDS mappings for O (e, g) and C (f, h) as well as images of the polished surfaces (i, j, k, l) with the corresponding C distribution (m, n, o, p).

lowest friction after polishing, even if this effect cannot be evaluated as significant due to the high variance. We assume that pyrolyzed residues from the POM binder act as a solid lubricant. In contrast to the other processes, these show more adhesive wear with some clearly visible smearing (Fig. 8l and p). Another indication of the improved frictional behavior in dry running is the fact that the MEAM samples did not exhibit higher wear despite their very low hardness compared to the counter body. In general, adhesion and abrasion can be observed in the dry polished tests, with the latter predominating in the reference, ADAM, and LPBF tests (Fig. 8i–k). Oxidative effects are also present, which is clearly shown in the signatures of the Raman analysis (Fig. 8q). Compared to LPBF, the MEX processes also show more pronounced carbon signatures, which can also be attributed to binder residues.

Apart from ADAM, both the other processes and the reference tended to increase COF and wear on untreated and laser-polished (LPBF) surfaces. This seems to be expected in view of the considerably rougher surface, which favors abrasive wear. However, the effect is only significant for reference due to the variance in the AM samples. Another interesting aspect is the variance in the repeatability tests. This can be explained by the variance of the surface topography determined in the PCA, which was significantly more pronounced for LPBF and MEAM and shows that the reproducibility of tribological tests plays an even more important role in the field of AM.

As expected, friction and wear were significantly reduced in all cases in the lubricated tests. After polishing, the ADAM samples exhibited a significantly lower (Wilcoxon rank sum test) COF than the reference. In contrast to all other conditions, there was reproducibly no measurable wear on the polished ADAM samples. After the test, the slightly deformed friction track could only be made visible qualitatively using white light interferometry (Fig. 8b). This effect could be attributed to the special fine porous surface (Fig. 8f), which possibly favors the EHL contact conditions in the mixed lubrication regime. In all other samples, abrasive wear with clearly visible grooving (Fig. 8a–c, d) was clearly dominant. In the case of MEAM (Fig. 8h), smearing was again observed, indicating the low hardness of the material combined with binder residues. The lubricated tests also showed clear carbonyl signatures in Raman analysis indicating PAO residues.

For all investigated conditions, the wear volume of the flat specimen exceeded that of the 100Cr6 counter body. This behavior is expected considering the substantially higher hardness of the counter body (≥61 HRC) compared to the investigated 17-4 PH materials. Although the ratio between specimen and ball wear appeared to vary between manufacturing routes and lubrication conditions, no systematic relationship could be established with sufficient confidence due to the experimental scatter. Therefore, the observed differences in wear partitioning should be interpreted with caution. As the wear was significantly lower in the lubricated tests and the AM surfaces were smoothed less over the test period, so that more mixed and boundary friction is present, the COF is significantly higher in all untreated AM samples compared to the polished state. Friction was lowest with MEAM samples, which could also be due to the supporting lubricating effect of binder residues in the protruding surface areas with mixed and boundary friction. Despite the low hardness, the wear was still comparatively low there as well as in the polished state.

3.5. *Electrochemical characterization*

The results of electrochemical characterization are summarized in Fig. 9. All samples showed a variation of OCP (Fig. 9a) reaching a value between −130 and −180 mV vs Ag|AgCl. The bulk reference exhibited a steady drift to nobler values similar to that of ADAM, although the latter trend reverted toward cathodic values after approximately 30 min.

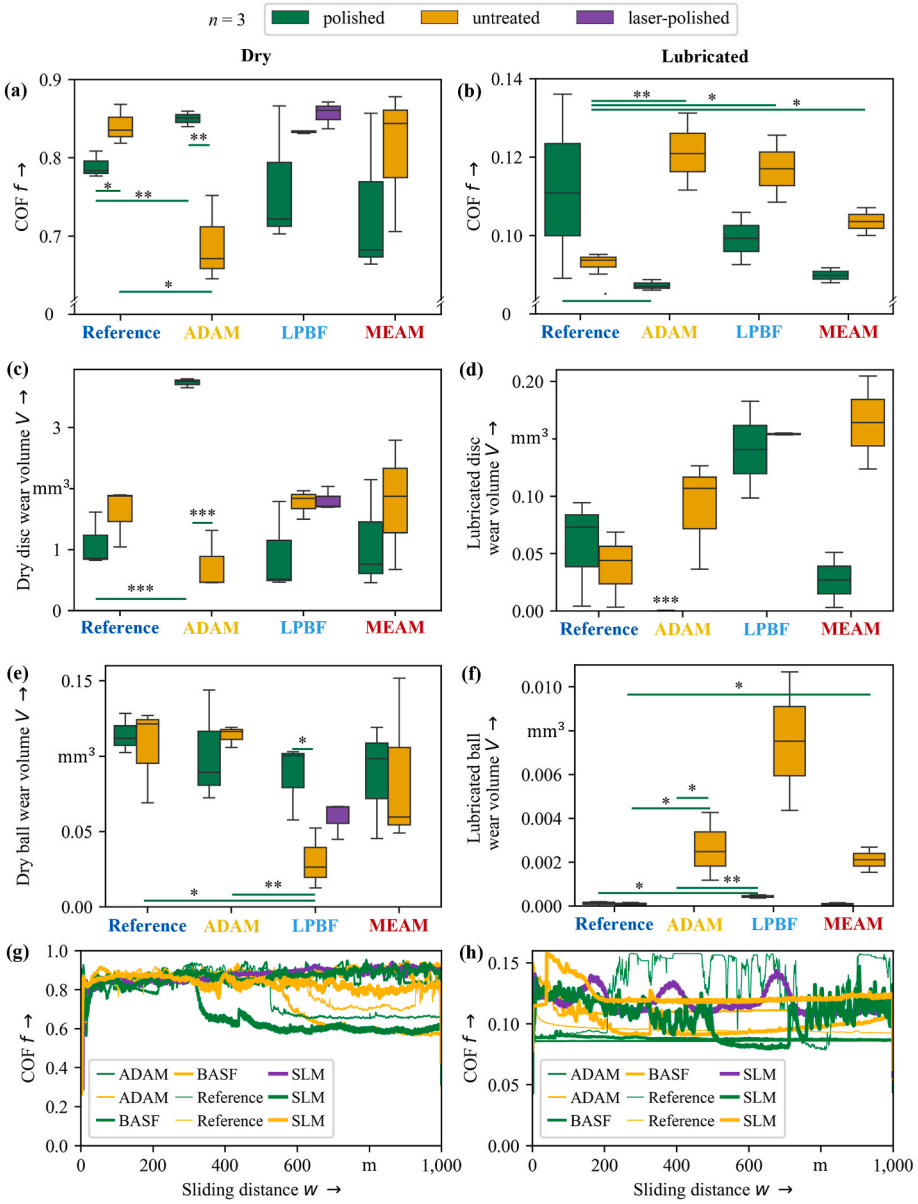


Fig. 7. Results of the tribometer tests: Mean coefficient of friction unlubricated (a) and lubricated (b) with the corresponding wear volumes of the test specimens (c, d) and the wear volumes of the 100Cr6 balls (e, f). Examples of friction curves for the first repeat test in each case (g, h). Selected significance levels (.: $p < 0.1$, *: $p < 0.05$, **: $p < 0.01$, ***: $p < 0.001$) from two-sided t-test for unpaired samples. Please note the different axis scaling.

Whereas, the LPBF and MEAM samples displayed OCP oscillations indicative of surface non-steadiness [42]. None of the polarization curves started at the last value of OCP, which is typical of pseudo-passivation typically observed for 17-4-PH steel in chloride containing media [43–45] and associated with metastable pitting [46].

The as-fabricated samples showed a similar cathodic response, whereas anodic polarization revealed the lowest and most stable passive current on the reference sample with passivity breakdown at the most noble potential. The presence of pitting was observed in all samples but only the reference has a marked pitting potential, which indicates that the passive layer on the AM samples is unstable or uneven. The LPBF material was found the least resistant to pitting, resulting in macroscopic pits (data not shown). The anodic response after mechanical polishing was similar to the as-fabricated state, except for the LPBF sample on which the effect of polishing resulted in lowering of the passive current.

The electrochemical trends can be explained by the process-dependent surface and subsurface characteristics revealed by microstructure analysis. First, the pore size, distribution, and interconnectivity inherent to each AM process are generally relevant for pit initiation and pitting stability of stainless steel [47]. Large, surface-connected cavities create locally aggressive microenvironments by concentrating chloride, restricting oxygen transport, and acidifying the occluded electrolyte resulting in destabilization of the passive film and thus lowering the threshold for passivity breakdown. This effect is observed in the earlier and more severe pitting on the LPBF sample. In contrast, the numerous but smaller pores in ADAM sample and the regularly distributed pores in MEAM disperse electrochemical activity across many sites, promoting predominantly metastable pitting rather than the rapid transition to stable pit growth.

The oxide-layer depth and chemical heterogeneity revealed by GDOES further correlate with the observed polarization behavior. All AM samples display a deeper and less uniform near-surface oxide layer as compared to the reference, consistent with the presence of pores intersecting the surface (see Fig. 5). For ADAM and MEAM, the oxygen-rich layer extends approximately 50 nm and 100 nm, respectively, and the carbon profiles exhibit undercut geometries, where a small surface

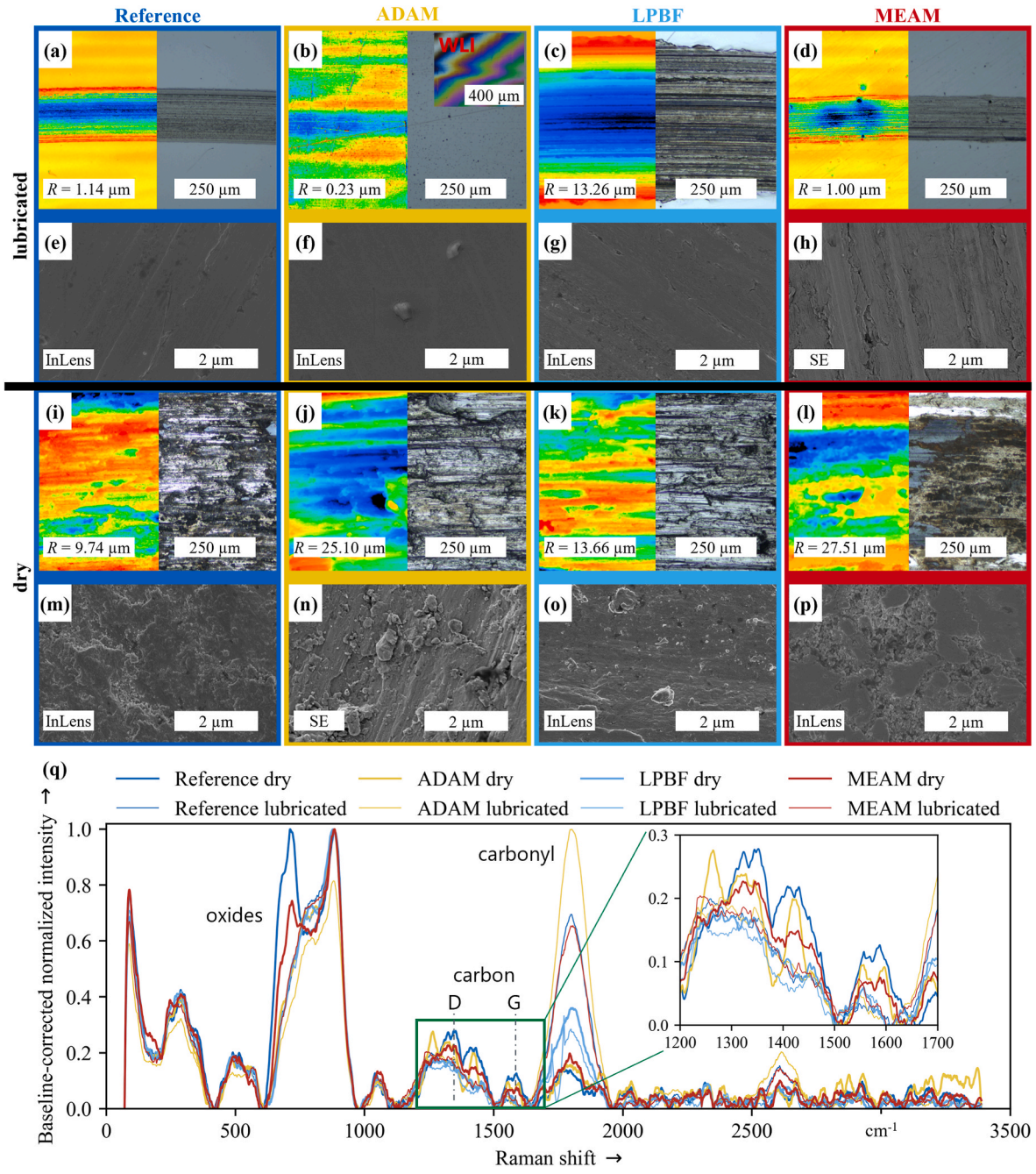


Fig. 8. Light and laser microscopic representative images of the wear track (e.g., (a)) as well as high-resolution SEM micrographs (e.g., (e)) of the lubricated (a-h) and dry (i-p) tests on polished samples. Due to the very different scales, the LSM profiles are normalized to the respective minima and maxima and the range R is given. The white light interferometric image for ADAM lubricated (b) illustrates the wear track that is otherwise not visible. Additional Raman analysis of the wear tracks showing oxidation, lubricant related signatures and differences in carbon phase.

opening leads into a wider subsurface pore. These features can trap electrolyte and chloride ions, providing sites for distributed metastable pit events without necessarily supporting rapid pit propagation. In LPBF, however, oxide and chemistry heterogeneity tends to be concentrated around fewer, larger defects, which both impair repassivation and accelerate pit growth, in agreement with the more pronounced and earlier breakdown observed in the anodic scans.

Finally, the effect of mechanical polishing aligns with the differences in passive-film stability. Polishing reduces surface roughness and removes shallow open pores, thereby lowering passive current, most notably in LPBF. Nonetheless, subsurface or partially buried defects (Fig. 5) remain electrochemically active translating to the pitting susceptibility the AM materials after polishing. The persistence of pits at comparatively low potentials in the polished AM samples is therefore crucial for the protectiveness of the passive-film. However, all materials have a similar response to repassivation.

4. Conclusions

This intensive experimental study compared the tribological and surface-related performance of 17-4 PH produced by LPBF, ADAM, and MEAM, including both untreated and polished states, and benchmarked them against a conventionally manufactured reference. The analysis integrated surface topography, microstructure, hardness, friction, wear,

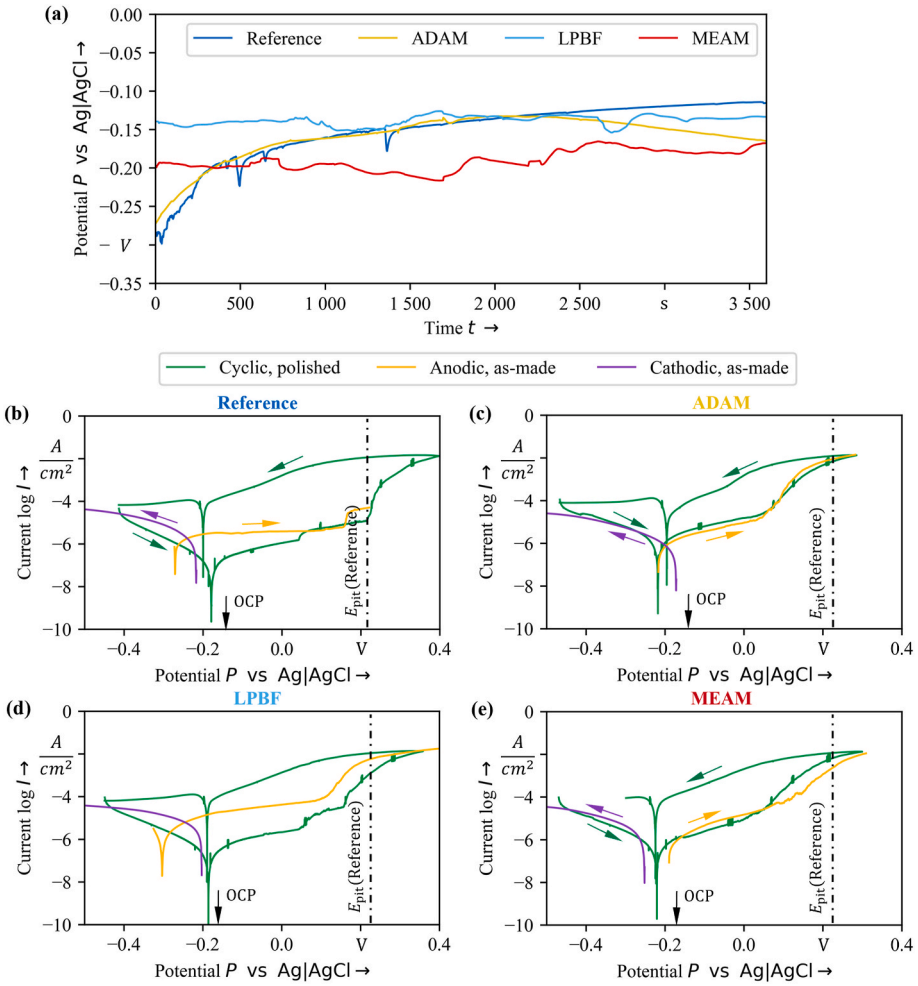


Fig. 9. Summary of electrochemical characterization: (a) OCP recorded for 1 h, Cathodic polarization and anodic polarization of the as-fabricated samples, and cyclic polarization of mechanically polished samples for (b) Reference, (c) ADAM, (d) LPBF and (e) MEAM. For convenience, OCP at the end of stabilization and the value of pitting potential of the reference sample are included in each plot.

and corrosion behavior to assess how process-induced differences affect tribological performance. The key findings can be summarized as follows:

- Surface characteristics of as-made material varied significantly across AM techniques. LPBF results in melt pool structures with occasional defects (due to lack of fusion and keyhole), ADAM showed fine homogeneous porosity, and MEAM exhibited larger, less uniformly distributed pores. Polishing reduced topographical differences, but statistical analysis revealed that process-specific signatures remained. ADAM showed the most regular surfaces, while MEAM exhibited the highest deviation due to print irregularities.
- Mechanical properties were strongly influenced by porosity and microstructure. ADAM reached the highest macroscopic and microscopic hardness, exceeding the reference, while MEAM showed the lowest macroscopic hardness associated with high porosity. LPBF achieved the highest bulk density among the AM samples but did not outperform ADAM in hardness.
- Dry sliding tests in ball-on-disc configuration against 100Cr6 showed increased friction and wear for ADAM samples despite being the hardest of the set, likely due to sharp surface peaks causing particle-induced third-body-wear. LPBF and MEAM samples performed comparably to the reference, with LPBF tending to oxidize more. MEAM samples tended to show the lowest friction, probably due to residual binder acting as a solid lubricant.
- Lubricated with PAO-40, friction and wear were significantly reduced for all samples with abrasive wear being the dominant wear mechanism. Polished ADAM samples showed the best performance with negligible wear, likely benefiting from its fine porosity that supported mixed friction EHL. MEAM samples again showed low friction and wear, supporting the hypothesis of a lubrication-enhancing surface residue also in mixed and boundary friction.
- Corrosion resistance of all the AM samples was lower compared to reference, attributed to surface porosity and oxide layer irregularities. LPBF samples exhibited the earliest pitting onset. Mechanical polishing slightly improved passivation, particularly for LPBF samples, but pitting susceptibility remained higher than in reference.

As a conclusion, the tribological and corrosion performance is highly process-dependent, even within a single alloy system. The results demonstrate that manufacturing route, surface morphology, porosity, and microstructure can significantly affect friction, wear, and corrosion behavior despite nearly identical chemical compositions. These findings contribute to the fundamental understanding of process-structure-tribology relationships in additively manufactured metallic materials and may provide guidance for future investigations under application-specific operating conditions. While the present study was conducted on 17-4 PH stainless steel, several of the observed effects are directly related to process-specific characteristics such as porosity, surface morphology, and residual binder, which are also encountered in other additively manufactured metallic alloy systems. Surface morphology

and porosity dominate over bulk hardness in determining friction and wear, particularly in unlubricated, i.e. technically dry, conditions. In the lubricated condition, fine porosity and uniform surfaces, as found for ADAM, can significantly enhance performance. This study demonstrated that MEX-based processes, particularly ADAM, can offer competitive or superior tribological behavior under lubrication despite lower bulk density. From a practical standpoint, MEX offers lower production costs, but has higher residual porosity compared to LPBF, which offers near-complete density at higher costs. MEX may therefore be suitable for cost-sensitive replacement parts or custom components in corrosion-prone applications such as pumps, valves, or maritime systems, while LPBF is advantageous for highly stressed precision components that require maximum density and mechanical reliability. However, the corrosion performance and process reproducibility of the MEX processes require further improvement. LPBF remains advantageous in terms of bulk density, but it is more susceptible to pitting corrosion. Further, the statistical surface analysis framework presented here enables robust comparisons between different AM processes and provides fundamentals for process selection based on application-specific tribological requirements. Future work should address long-term tribological performance under dynamic loading in a corrosive environment, and refined understanding of the process-structure-property interactions to guide AM component design for tribological applications. In addition, the systematic investigation of standardized post-processing heat treatments (e.g., H900) across different AM routes is required to clarify their influence on tribological and corrosion performance.

CRediT authorship contribution statement

Christian Orgeldinger: Writing – original draft, Visualization, Validation, Software, Methodology, Investigation, Formal analysis, Data curation, Conceptualization. **Armin Seynstahl:** Methodology, Formal analysis, Conceptualization. **Tobias Rosnitschek:** Writing – review & editing, Resources. **Jorge Ramos Grez:** Writing – review & editing, Resources. **Magdalena Walczak:** Writing – original draft, Resources, Investigation, Formal analysis, Data curation. **Max Marian:** Writing – original draft, Supervision, Resources, Methodology, Investigation, Formal analysis, Data curation, Conceptualization. **Stephan Tremmel:** Writing – review & editing, Supervision, Resources, Methodology.

Funding

This research received no external funding.

Declaration of competing interest

The authors declare that they have no known competing financial interests or personal relationships that could have appeared to influence the work reported in this paper.

Acknowledgments

C. Orgeldinger, A. Seynstahl, T. Rosnitschek, and S. Tremmel greatly acknowledge the continuous support of the University of Bayreuth. J. Ramos-Grez acknowledges the financial support given by ANID-Chile within the project Fondequip EQM 180081. M. Marian greatly acknowledges the financial support from the Vicerrectoría Académica (VRA) of the Pontificia Universidad Católica de Chile within the Programa de Inserción Académica (PIA) and INICIO 2024-19 as well as from Schaeffler FAG Foundation within the Future Technology Award 2022. Furthermore, the authors would like to thank Hans Lassner-Meisel from Metals and Alloys at the University of Bayreuth for his support with the metallographic sample preparation and microindentation. The authors thank Lena Geiling and Daniel Leykam from Electrochemical Process Engineering at the University of Bayreuth for supporting the SEM, EDS and Raman measurements and the Bavarian Polymer Institute for the use of the SEM. Additionally, Dr. Tobias Rödlmeier from BASF 3D Printing Solutions is thanked for his support with printing and sintering of the MEAM specimens.

Data availability

All original data including surface data, microscope images and measurement data (friction and wear) are made available. These can be found at Zenodo under (Zenodo link with DOI will be added to the publication).

References

[1] A. Behera, Processes and application in additive manufacturing: practices in aerospace, automobile, medical, and electronic industries, in: K. R. Balasubramanian, V. Senthilkumar (Eds.), Advances in Civil and Industrial Engineering, IGI Global, 2020, pp. 25–47, https://doi.org/10.4018/978-1-7998-4054-1.ch002.
[2] H.A. Colorado, E.I.G. Velásquez, S.N. Monteiro, Sustainability of additive manufacturing: the circular economy of materials and environmental perspectives, J. Mater. Res. Technol. 9 (2020) 8221–8234, https://doi.org/10.1016/j.jmrt.2020.04.062.
[3] D. Herzog, V. Seyda, E. Wycisk, C. Emmelmann, Additive manufacturing of metals, Acta Mater. 117 (2016) 371–392, https://doi.org/10.1016/j.actamat.2016.07.019.
[4] J. Jones, A. Vafadar, R. Hashemi, A review of the mechanical properties of 17-4PH stainless steel produced by bound powder extrusion, J. Manuf. Mater. Process. 7 (2023) 162, https://doi.org/10.3390/jmmp7050162.
[5] Z. Lotfizarei, A. Mostafapour, A. Barari, A. Jalili, A.E. Patterson, Overview of debinding methods for parts manufactured using powder material extrusion, Addit. Manuf. 61 (2023) 103335, https://doi.org/10.1016/j.addma.2022.103335.
[6] C. Lieberwirth, M. Sarhan, H. Seitz, Mechanical properties of stainless-steel structures fabricated by composite extrusion modelling, Metals 8 (2018) 84, https://doi.org/10.3390/met8020084.
[7] C. Orgeldinger, A. Seynstahl, T. Rosnitschek, S. Tremmel, Surface properties and tribological behavior of additively manufactured components: a systematic review, Lubricants 11 (2023) 257, https://doi.org/10.3390/lubricants11060257.
[8] S.M. Kelly, S.L. Kampe, Microstructural evolution in laser-deposited multilayer Ti-6Al-4V builds: part II. Thermal modeling, Metall. Mater. Trans. A 35 (2004) 1869–1879, https://doi.org/10.1007/s11661-004-0095-7.
[9] Z. Wang, T.A. Palmer, A.M. Beese, Effect of processing parameters on microstructure and tensile properties of austenitic stainless steel 304L made by directed energy deposition additive manufacturing, Acta Mater. 110 (2016) 226–235, https://doi.org/10.1016/j.actamat.2016.03.019.
[10] J.K. Patel, B. Wilshire, The challenge to produce consistent mechanical properties in Nb-HSLA strip steels, J. Mater. Process. Technol. 120 (2002) 316–321, https://doi.org/10.1016/S0924-0136(01)01130-X.
[11] Y. Zhu, X. Tian, J. Li, H. Wang, The anisotropy of laser melting deposition additive manufacturing Ti–6.5Al–3.5Mo–1.5Zr–0.3Si titanium alloy, Mater. Des. 67 (2015) 538–542, https://doi.org/10.1016/j.matdes.2014.11.001.
[12] A.M. Ralls, P. Kumar, P.L. Menezes, Tribological properties of additive manufactured materials for energy applications: a review, Processes 9 (2021) 31, https://doi.org/10.3390/pr9010031.
[13] R. Shah, N. Pai, A. Rosenkranz, K. Shirvani, M. Marian, Tribological behavior of additively manufactured metal components, JMMP 6 (2022) 138, https://doi.org/10.3390/jmmp6060138.
[14] Y. Zhu, B. Raeymaekers, M. Khonsari (Eds.), Special issue on tribology of additive manufacturing, J. Tribol. 143 (2021) 050201, https://doi.org/10.1115/1.4050943.
[15] R. Shah, M. Woydt, N. Huq, A. Rosenkranz, Tribology meets sustainability, ILT 73 (2021) 430–435, https://doi.org/10.1108/ILT-09-2020-0356.
[16] N. Ur Rahman, D.T.A. Matthews, M. de Rooij, A.M. Khorasani, I. Gibson, L. Cordova, et al., An overview: laser-based additive manufacturing for high temperature tribology, Front. Mech. Eng. 5 (2019) 16, https://doi.org/10.3389/fmech.2019.00016.
[17] S. Bagherifard, N. Beretta, S. Monti, M. Riccio, M. Bandini, M. Guagliano, On the fatigue strength enhancement of additive manufactured AlSi10Mg parts by mechanical and thermal post-processing, Mater. Des. 145 (2018) 28–41, https://doi.org/10.1016/j.matdes.2018.02.055.
[18] A.R. Balachandramurthi, J. Moverare, N. Dixit, R. Pederson, Influence of defects and as-built surface roughness on fatigue properties of additively manufactured Alloy 718, Mater. Sci. Eng., A 735 (2018) 463–474, https://doi.org/10.1016/j.msea.2018.08.072.
[19] J.A. Ramos-Grez, I.L. Fé-Pérdomo, N. Yu, In situ surface laser polishing of laser powder bed fusion 316L steel flat specimens. XV Lamdamap Conference Laser Metrology and Machine Performance, Edinburgh, Scotland, UK, 2023.
[20] N. Worts, J. Jones, J. Squier, Surface structure modification of additively manufactured titanium components via femtosecond laser micromachining, Opt. Commun. 430 (2019) 352–357, https://doi.org/10.1016/j.optcom.2018.08.055.
[21] L. Hackel, J.R. Rankin, A. Rubenchik, W.E. King, M. Matthews, Laser peening: a tool for additive manufacturing post-processing, Addit. Manuf. 24 (2018) 67–75, https://doi.org/10.1016/j.addma.2018.09.013.

[22] H. Attar, M.J. Bermingham, S. Ehtemam-Haghighi, A. Dehghan-Manshadi, D. Kent, M.S. Dargusch, Evaluation of the mechanical and wear properties of titanium produced by three different additive manufacturing methods for biomedical application, Mater. Sci. Eng., A 760 (2019) 339–345, https://doi.org/10.1016/j.msea.2019.06.024.

[23] H. Li, Z.W. Chen, M. Ramezani, Effect of temperature on sliding wear behavior of Ti-6Al-4V alloy processed by powder bed fusion additive manufacturing techniques, J of Materi Eng and Perform 31 (2022) 8940–8954, https://doi.org/10.1007/s11665-022-06959-2.

[24] C. García-Hernández, J.A. Naranjo, M.Á. Castro-Sastre, C. Berges, A.I. Fernandez-Abia, F. Martín-Pedrosa, et al., Enhancing wear performance: a comparative study of traditional vs. additive manufacturing techniques for 17–4pH SS, Wear 540–541 (2024) 205258, https://doi.org/10.1016/j.wear.2024.205258.

[25] R.F. Schaller, J.M. Taylor, J. Rodelas, E.J. Schindelholz, Corrosion properties of powder bed fusion additively manufactured 17-4 PH stainless steel, Corrosion 73 (2017) 796–807, https://doi.org/10.5006/2365.

[26] M.H. Nie, S. Zhang, Z.Y. Wang, T.Y. Yin, C.H. Zhang, C.L. Wu, et al., Laser cladding of 17-4 PH stainless steel coatings: microstructure, texture characterization, and corrosion resistance, J of Materi Eng and Perform 32 (2023) 5545–5553, https://doi.org/10.1007/s11665-022-07484-y.

[27] J.R.J. Michla, R. Nagarajan, S.O. Ismail, T. Ramprabhu, S. Siengchin, M. P. Indiradevi, et al., Corrosion behaviours of additively manufactured nitrided 17–4 PH steels in different environments, Trans. Indian Inst. Met. 76 (2023) 1863–1873, https://doi.org/10.1007/s12666-023-02884-7.

[28] J.R.J. Michla, C.R. Rajkumar, Corrosion behaviour of nitroxy-QPQ additively manufactured 17-4 PH steel on marine and nuclear reactor components, Surf. Eng. 40 (2024) 1113–1120, https://doi.org/10.1177/02670844241287344.

[29] DIN EN ISO 6508-1, Metallische Werkstoffe –Härteprüfung Nach Rockwell –Teil 1: Prüfverfahren (ISO 6508-1:2023); Deutsche Fassung EN ISO 6508-1:2023 n.d.

[30] DIN EN ISO 14577-1, Metallische Werkstoffe –Instrumentierte Eindringprüfung Zur Bestimmung Der Härte Und Anderer Werkstoffparameter –Teil 1: Prüfverfahren (ISO/DIS 14577-1:2024); Deutsche Und Englische Fassung Pren ISO 14577-1:2024 n.d.

[31] DIN EN ISO 25178-2:2023-09, Geometrische Produktspezifikation_(GPS)_-Oberflächenbeschaffenheit: Flächenhaft_- Teil_2: Begriffe Und Kenngrößen Für Die Oberflächenbeschaffenheit (ISO_25178-2:2021); Deutsche Fassung EN_ISO_25178-2:2022 n.d. https://doi.org/10.31030/3294021.

[32] G. Singh, J.-M. Missiaen, D. Bouvard, J.-M. Chaix, Additive manufacturing of 17–4 PH steel using metal injection molding feedstock: analysis of 3D extrusion printing, debinding and sintering, Addit. Manuf. 47 (2021) 102287, https://doi.org/10.1016/j.addma.2021.102287.

[33] M. Galati, P. Minetola, Analysis of density, roughness, and accuracy of the Atomic Diffusion Additive Manufacturing (ADAM) process for metal parts, Materials 12 (2019) 4122, https://doi.org/10.3390/ma12244122.

[34] A. Kudzal, B. McWilliams, C. Hofmeister, F. Kellogg, J. Yu, J. Taggart-Scarff, et al., Effect of scan pattern on the microstructure and mechanical properties of powder bed fusion additive manufactured 17-4 stainless steel, Mater. Des. 133 (2017) 205–215, https://doi.org/10.1016/j.matdes.2017.07.047.

[35] Z. Hu, H. Zhu, H. Zhang, X. Zeng, Experimental investigation on selective laser melting of 17-4PH stainless steel, Opt Laser. Technol. 87 (2017) 17–25, https://doi.org/10.1016/j.optlastec.2016.07.012.

[36] M.R. Condruz, A. Paraschiv, C. Puscasu, HEAT TREATMENT INFLUENCE ON HARDNESS AND MICROSTRUCTURE OF ADAM MANUFACTURED 17-4 PH, 2018.

[37] A.D. Akessa, W.M. Tucho, H.G. Lemu, J. Grønsund, Investigations of the microstructure and mechanical properties of 17-4 PH ss printed using a MarkForged metal X, Materials 15 (2022) 6898, https://doi.org/10.3390/ma15196898.

[38] V. Di Pompeo, E. Santecchia, A. Santoni, K. Sleem, M. Cabibbo, S. Spigarelli, Microstructure and defect analysis of 17-4PH stainless steel fabricated by the bound metal deposition additive manufacturing technology, Crystals 13 (2023) 1312, https://doi.org/10.3390/cryst13091312.

[39] A. Go, E.S. Jeon, S.K. Moon, S.J. Park, Fabrication of 17-4PH stainless steel by metal material extrusion: effects of process parameters and heat treatment on physical properties, Mater. Des. 248 (2024) 113471, https://doi.org/10.1016/j.matdes.2024.113471.

[40] Y.-H. Cho, S.-Y. Park, J.-Y. Kim, K.-A. Lee, 17-4PH stainless steel with excellent strength–elongation combination developed via material extrusion additive manufacturing, J. Mater. Res. Technol. 24 (2023) 3284–3299, https://doi.org/10.1016/j.jmrt.2023.03.228.

[41] L.E. Murr, E. Martinez, J. Hernandez, S. Collins, K.N. Amato, S.M. Gaytan, et al., Microstructures and properties of 17-4 PH stainless steel fabricated by selective laser melting, J. Mater. Res. Technol. 1 (2012) 167–177, https://doi.org/10.1016/S2238-7854(12)70029-7.

[42] P. Forcellese, W.A. Khan, T. Mancia, M. Simoncini, M. Reiser, M. Kouřil, et al., Corrosion resistance properties of As-Sintered 17-4 PH samples additive-manufactured through binder jetting, Metals 15 (2025) 1082, https://doi.org/10.3390/met15101082.

[43] S.S. Poor Mousavi, M. Seyedi, M.-H. Moayed, M. Mirjalili, I. Taji, Mortazavi S. Hosein, High potential inhibition of the 17-4 PH stainless steel in the presence of nitrate and evolution of metastable pitting, Corrosion 79 (2023) 964–972, https://doi.org/10.5006/4281.

[44] T.O. Olugbade, Passivation behaviour of surface-treated 17-4PH stainless steel in chloride-containing environment with varying concentrations, Chem. Afr. 5 (2022) 333–340, https://doi.org/10.1007/s42250-022-00312-9.

[45] J. Villegas-Tovar, C. Gaona-Tiburcio, M. Lara-Banda, E. Maldonado-Bandala, M. A. Baltazar-Zamora, J. Cabral-Miramontes, et al., Electrochemical corrosion behavior of passivated precipitation hardening stainless steels for aerospace applications, Metals 13 (2023) 835, https://doi.org/10.3390/met13050835.

[46] B. Martínez-Aparicio, D. Martínez-Bastidas, C. Gaona-Tiburcio, U. Martin, J. Cabral-Miramontes, F. Almeraya-Calderón, Localized corrosion of 15–5 PH and 17–4 PH stainless steel in NaCl solution, J. Solid State Electrochem. 27 (2023) 2993–3001, https://doi.org/10.1007/s10008-023-05593-9.

[47] M. Laleh, A.E. Hughes, W. Xu, I. Gibson, M.Y. Tan, A critical review of corrosion characteristics of additively manufactured stainless steels, Int. Mater. Rev. 66 (2021) 563–599, https://doi.org/10.1080/09506608.2020.1855381.